



Investigation of the metatetic reaction in iron-boron binary alloys

Kara E. Luitjohan*, Matthew John M. Krane, Volkan Ortalan, David R. Johnson

School of Materials Engineering, Purdue University, 701 West Stadium Ave, West Lafayette, IN 479005, United States

ARTICLE INFO

Article history:

Received 3 July 2017

Received in revised form

30 September 2017

Accepted 26 October 2017

Available online 27 October 2017

Keywords:

Metatetic reaction

Iron-boron binary alloy

Directional solidification

ABSTRACT

The use of advanced high strength steels, such as boron containing steels, in the automotive industry is enabling lighter weight vehicles leading to increased fuel economies. However, boron containing steels are difficult to commercially produce. Thermodynamic studies of the Fe-B system predict a metatetic reaction, $\delta \rightarrow L + \gamma$, to occur on the iron-rich side of the diagram. This would result in solid material remelting as the temperature is decreased, which could be the source of the casting defects. To experimentally investigate the predicted metatetic reaction, levitation zone melting is used to control the boron segregation in two simple Fe-B binary alloys, and confocal scanning laser microscopy allows for in-situ observation of local microstructural changes as temperature is varied. Both experimental methods show evidence of a metatetic reaction providing a good comparison to predicted phase diagrams. Based on the experimental results, the metatetic reaction occurs over a broader range of compositions than predicted with $C_s = 0.0025$ wt% B, $C_L = 2.0$ wt% B, and C_R ranging from approximately 0.03 to 0.06 wt% B.

© 2017 Elsevier B.V. All rights reserved.

1. Introduction

There is a current push in the automotive industry to increase the fuel economy of passenger vehicles. One way to achieve this increase is through the use of advanced high strength steels (AHSS). AHSS with yield strengths greater than 550 MPa allows for thinner gauge components to be implemented in vehicles without sacrificing safety, thereby lowering the weight of the vehicle and improving fuel economy [1]. Included under the umbrella of AHSS are boron-based hot formed (HF) steels. Typically HF steels contain between 0.002 and 0.005 wt% B [2]. Even in these small amounts, the addition of boron makes the steel difficult to commercially produce, specifically via continuous casting. Defects in the continuously cast boron containing steels include surface cracks, internal half way cracks, folds, pockets, ridges, and, in more severe cases, breakouts [3–5].

While the motivation behind the use of AHSS is clear, the causes and thus solutions to the casting defects caused by boron are presently unclear. In some thermodynamic studies of the iron-boron system, a $\delta + L \rightarrow \gamma$ peritectic reaction, such as that shown in Fig. 1a, is predicted [6]. However, in other investigations, a $\delta \rightarrow L + \gamma$ metatetic reaction is predicted [3,7]. This metatetic reaction results in a completely solid material partially remelting with a

decrease in temperature, Fig. 1b. Four predicted Fe-B phase diagrams found in literature are detailed in Table 1 including the reaction temperature, T_R , the reaction composition, C_R , the solid composition at T_R , C_s , and the liquid composition at T_R , C_L . The compositions and temperatures match to the locations labeled in Fig. 1. Three of the sources predict a metatetic reaction while one predicts a peritectic reaction [6–10]. The three predicted metatetic reactions differ on the compositions that undergo the reaction, specifically the minimum amount of boron that will cause remelting through the metatetic reaction. A recent diagram produced from the TCFE8 thermodynamic database (Thermo-Calc: Steels/Fe alloys database) predicts that a boron composition as low as 0.0025 wt% will remelt through the metatetic reaction [8,10]. Two older diagrams from Kubaschewski and the TCFE5 thermodynamic database predict the minimum amount of boron that will remelt at an order of magnitude larger than TCFE8, 0.039 wt% and 0.022 wt% respectively [7–9]. Also, the diagram from the TCFE5 database predicts post-metatetic remelting, $\gamma \rightarrow L + \gamma$, due to a retrograde solidus between compositions of 0.015 and 0.022 wt% B, unlike any of the other predicted diagrams [8,9]. It is evident that metatetic reaction and the corresponding solidification behavior is not well characterized in the Fe-B system.

This study utilizes levitation zone melting to experimentally investigate the low temperature remelting through the controlled segregation of boron. An early description of this process is given by B. F. Oliver [11]. The large range of compositions and microstructures contained in the zone melted ingot are characterized with

* Corresponding author.

E-mail address: kluitjoh@purdue.edu (K.E. Luitjohan).

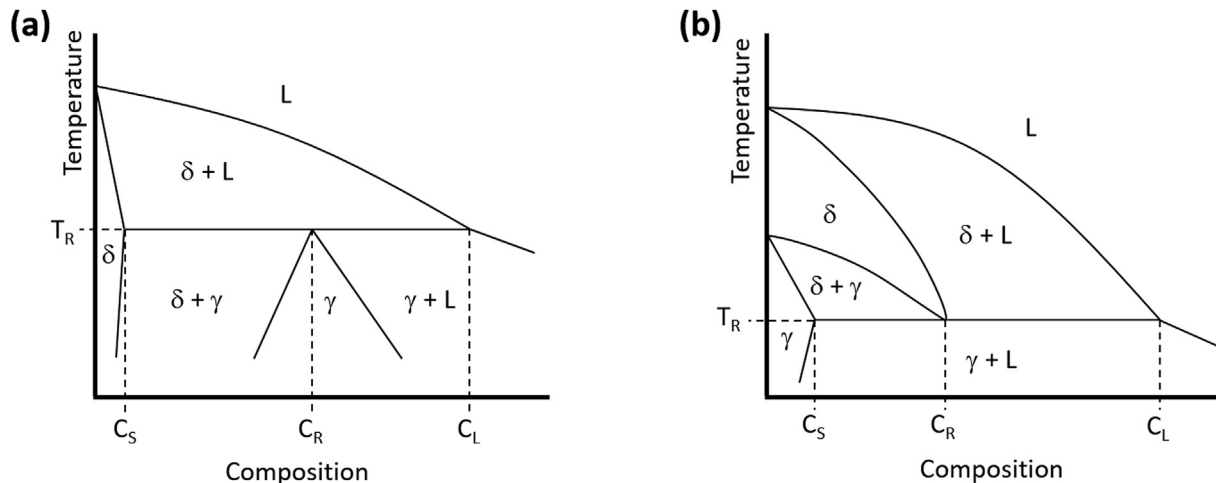


Fig. 1. Partial binary phase diagrams showing a typical (a) peritectic and (b) metatactic reaction occurring at composition C_R and temperature T_R .

Table 1

Comparison of the reaction temperature, T_R , the solid composition, C_S , the reaction composition, C_R , and the liquid composition, C_L , of four predicted Fe-B phase diagrams.

Reference	T_R (°C)	C_S (wt% B)	C_R (wt% B)	C_L (wt% B)	Reaction type
Rompaey et al. [6]	1396	0.00086	0.0020	1.7	Peritectic
Kubaschewski [7]	1381	0.039	0.097	1.5	Metatactic
Thermo-Calc TCFE5 database [9]	1360	0.022	0.045	2.1	Metatactic
Thermo-Calc TCFE8 database [10]	1384	0.0025	0.0097	2.1	Metatactic

optical microscopy and confocal scanning laser microscopy (CSLM). These experimental results are then compared to the predicted phase diagrams to better understand the remelting reactions.

2. Experimental technique

Two iron-boron alloys were analyzed for this study. A low boron alloy containing nominally 0.0168 wt% B was a 45 kg ingot cast in a vacuum induction furnace at the East Chicago (USA) Center of ArcelorMittal Global R&D. A high boron alloy containing nominally 0.045 wt% B was a 1 kg ingot cast in a small tilt-pour vacuum induction melter at Purdue University. After achieving vacuum, the furnace was backfilled with argon. The sample was melted in a zirconia crucible and cast into a chilled permeant Cu mold to produce 25 mm diameter samples for zone melting. In both alloys, electrolytic iron and vacuum induction melting was utilized to limit any impurities in the cast material.

Each alloy was levitation zone melted to create a large range of compositions and microstructures within each ingot. Levitation zone melting is a containerless processing method as illustrated in Fig. 2a. This process is similar to vertical float zone melting, however, at a ~25 mm diameter, surface tension is insufficient to shape and constrain the liquid zone between the two solid bars. The liquid zone would tend to roll over onto the lower solid bar resulting in a possible spill if only surface tension was relied upon [12]. In this process, an induction coil and eddy current plate assembly is used to melt, levitate, and shape the liquid zone to a height similar to that of the solid bar diameter, ~20 mm in this study. A melting solid/liquid interface is present at the top of the hot zone while a freezing solid/liquid interface is located at the bottom. The shape of the liquid zone and dimensions of the freezing solid/liquid interface are controlled by moving the top solid portion relative to the bottom. To maintain a smooth solid/liquid interface, the bottom solid bar is rotated [13]. This ingot rotation, along with induction stirring, contributes to a well-mixed liquid zone via turbulent flow [14]. In

this study, the zone melted ingot is moved through the assembly at a rate of ~12 mm/h.

The levitation zone melting process allows for the controlled segregation of solute elements with a large portion of the solute being swept towards the end of the bar. Depending on the partition coefficient, k , of the particular solute element, a single pass in the levitation zone melter will result in a composition profile such as those shown in Fig. 2b [15]. This composition profile can be divided into two distinct zones, the directionally solidified (DS) zone and the last zone to solidify. As the partition coefficient approaches unity, such as $k = 0.8$ in Fig. 2b, the DS zone can be further broken down into a transient zone, where initial solidification occurs, followed by a steady state zone where steady state planar solidification occurs at the original alloy composition, C_0 . When the partition coefficient is smaller, such as $k = 0.4$ and $k = 0.1$ in Fig. 2b, the composition of the whole DS zone is less than the original alloy composition, C_0 , with the solute balance residing in the last zone.

Predicted iron-boron phase diagrams show $k < 0.1$, so an expected composition profile from a single pass through the levitation zone melter is expected to look similar to the curve for $k = 0.1$ in Fig. 2b. The compositional gradient and microstructure from the zone melted ingot can also be used to investigate the differences in the predicted phase diagrams, Table 1. For example, an iron-boron alloy can be zone melted for a certain length to reach a specific target liquid composition for the last zone. The induction power can then be reduced, and, with an increased cooling rate, the solidification growth front will transition from planar to dendritic growth. Analysis of the microstructure, composition, morphology, and degree of microsegregation provides experimental evidence that can be compared to predicted phase diagrams.

While the last zone contains higher solute concentration compared to the DS zone it also solidifies faster, as mentioned previously. The cooling rate of the last zone for both alloys, as measured by a high temperature infrared pyrometer, was found to be ~54 °C/min. Similarly, the cooling rate of the DS zone was

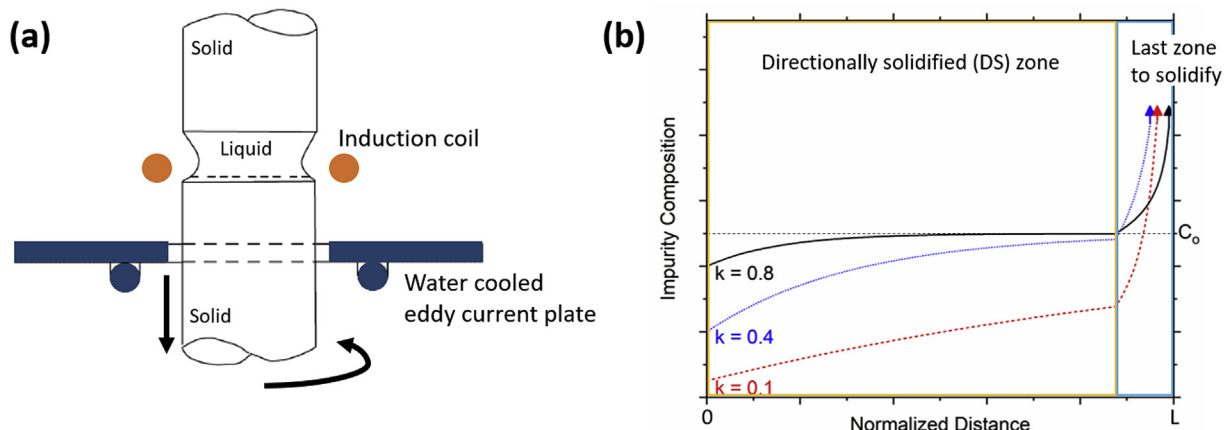


Fig. 2. (a) Schematic of the levitation zone melting process, and (b) typical composition profiles of a single pass zone melted ingot with various partition coefficients.

measured at ~ 3 °C/min with a thermal gradient through the solid/liquid interface of ~ 15 °C/mm. Before reducing the induction power, the directionally solidified bar well behind the molten zone should consist of the high temperature γ -fcc phase. Therefore, during the power down, the cooling rate through the γ -fcc to α -bcc phase fields should occur at a similar rate of ~ 54 °C/min.

To describe the microsegregation as the solidification growth front transitions to a dendritic microstructure in the last zone, the 1D Scheil equation is modified to allow for the partition coefficient, k , to vary as a function of temperature, T . The solute rejected from the freezing solid with a composition of $C'_{s,eq}$ is pushed into the

liquid which increases from composition $C_{L,eq}$ and fraction f_L to a new equilibrium composition of $C'_{L,eq}$ and fraction f'_L . Equalizing the amount of solute pushed out of the freezing solid to the amount of solute that must be increased in the liquid, the modified 1D Scheil equation takes the form of Eq. (1). For estimation purposes, solidification of δ -bcc can be approximated with $k' \approx 0.008$, and solidification of γ -fcc can be approximated with $k' \approx 0.001$.

$$f'_L = \frac{f_L(C'_{s,eq} - C_{L,eq})}{C'_{L,eq}(k' - 1)} \text{ where } k' = \frac{C'_{s,eq}}{C'_{L,eq}}$$
 (1)

Along each zone melted ingot, various regions were selected for bulk composition measurements using spark optical emission spectroscopy (OES) performed at the East Chicago (USA) Center of ArcelorMittal Global R&D. The various regions were also characterized with optical microscopy. Prior to imaging, the ingots were polished and, if necessary, etched with $\sim 3\%$ nital solution. To observe *in-situ* phase transformations and reaction temperatures, samples from the zone melted ingot were investigated in a confocal scanning laser microscope (CSLM) located at the East Chicago (USA) Center of ArcelorMittal Global R&D. The CSLM system utilizes a He-Ne laser for imaging and a halogen lamp for temperature control as

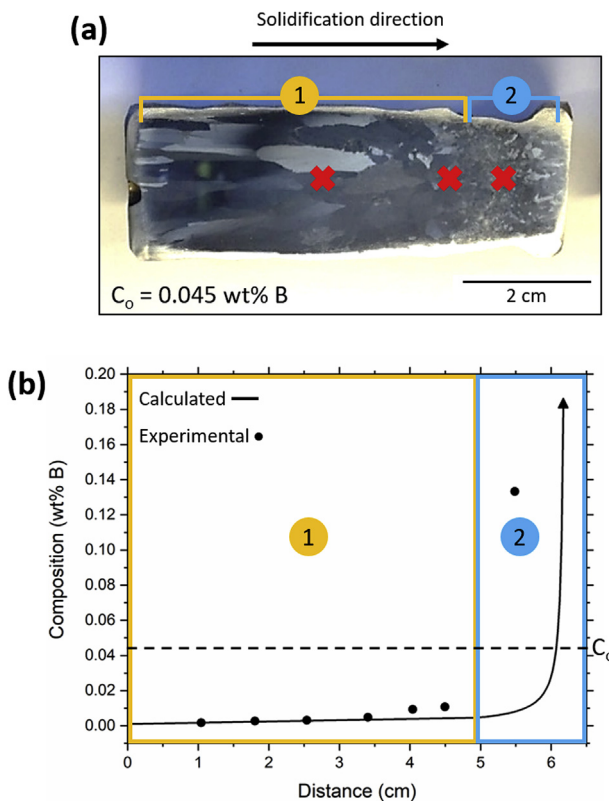


Fig. 3. (a) Image and (b) composition profile of the high boron alloy after zone melting. The solid line is the calculated composition while the circles represent the experimental measurements. The directionally solidified (DS) zone is labeled 1, and the last zone to solidify is labeled 2.

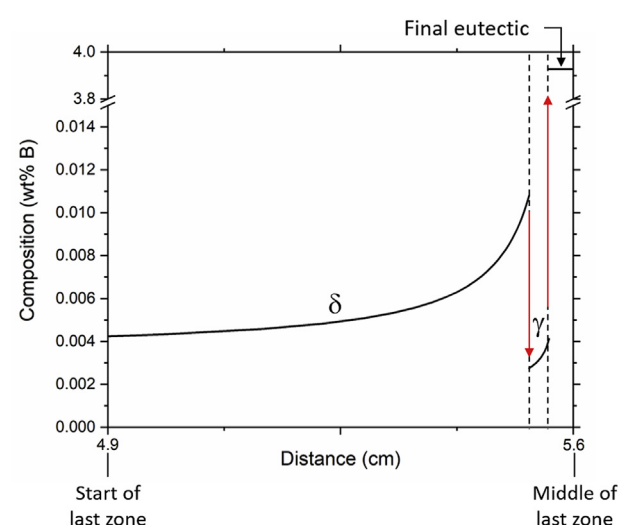


Fig. 4. The composition profile of the last zone to solidify from the zone melt of the high boron alloy utilizing the 1D Scheil equation.

Table 2

Average compositions and phase fractions present in the last zone to solidify calculated from a 1D Scheil equation and the Thermo-Calc TCFE8 database.

Low Boron Alloy		High Boron Alloy	
$\bar{C}_{LastZone} = 0.033 \text{ wt\% B}$	$\bar{C}_{LastZone} = 0.21 \text{ wt\% B}$	Avg. wt\% B	Fraction Solid (%)
$\delta\text{-bcc iron}$	0.0040	98.7	0.0054
$\gamma\text{-fcc iron}$	0.0032	0.604	0.0032
Eutectic	3.9	0.748	3.9

described in detail by Chikama et al. [16]. Three sections from the zone melt of the high boron alloy including a low boron region from the DS zone, a mid-boron region from the start of the last zone, and a high boron region from the middle of the last zone were studied in the CSLM. For all image analysis, ImageJ was utilized [17].

3. Results

The high boron and low boron alloys were machined into ~25 mm diameter bars and levitation zone melted. Two distinct regions can be seen after polishing and etching of the zone melted alloy, such as those seen in the zone melted high boron alloy in Fig. 3a. The DS zone, labeled 1, contains long columnar grains while smaller, equiaxed grains are present in the last zone to solidify, labeled 2. In Fig. 3b, the calculated composition profile of the high boron alloy from the Thermo-Calc TCFE8 database is represented by a solid line [10,15]. The calculated profile does not differ greatly if the older TCFE5 database is used [9]. The circles along the composition profile in Fig. 3b show experimental measurements obtained from spark OES. The experimental measurements match with the calculated profile. For the last zone, the average calculated compositions were ~0.033 wt% B for the low boron alloy and ~0.205 wt% B for the high boron alloy. The experimentally measured compositions in the last zone were 0.033 wt% B for the low boron alloy and 0.133 wt% B for the high boron alloy.

To investigate the microsegregation in the last zone to solidify, the 1D Scheil equation, Eq. (1), and the Thermo-Calc TCFE8 database was applied to the zone melted high boron alloy. With a starting composition of 0.205 wt% B, the calculated composition profile of the last zone is shown in Fig. 4. According to the calculations, a majority of the last zone, 90.5%, should solidify as $\delta\text{-bcc}$ iron. At the metatectic temperature, the new $\gamma\text{-fcc}$ iron that begins to form will contain less boron than the previous $\delta\text{-bcc}$ iron. The

final fraction of liquid that remains at 1175 °C will form a binary eutectic structure composed of $\gamma\text{-fcc}$ iron and Fe_2B . The calculations predict that only 4.27% of the total solid in the last zone will solidify as $\gamma\text{-fcc}$ iron while 5.19% will freeze as the binary eutectic.

The calculated data from both zone melted alloys are shown in Table 2. Similar to the last zone in the high boron alloy, the calculations for the last zone in the low boron alloy show that it solidifies as mostly $\delta\text{-bcc}$ iron with small amounts of $\gamma\text{-fcc}$ iron and binary eutectic. The phase fractions calculated for both alloys are similar to the values calculated from the older Thermo-Calc TCFE5 database. The major difference in the calculations between the two databases are the average boron concentrations in each phase with the recent TCFE8 database predicting less boron in the $\delta\text{-bcc}$ and $\gamma\text{-fcc}$ iron phases and more boron in the eutectic.

The optical images in Fig. 5 show the last zone to solidify from both zone melted alloys. In both alloys, Fe_2B can be seen along the grain boundaries from the eutectic reaction and as small spherical particles within the bulk of the structure from the metatectic reaction. The amount of eutectic structure, marked by the arrows in Fig. 5, is higher in the high boron alloy, as predicted with the Scheil equation. Note the Fe_2B particles in the bulk of the grains, the array of small dark dots, are expected to have resulted from the metatectic reaction which will be discussed later.

To further investigate the phase transitions occurring throughout the zone melted ingot, samples from various locations along the zone melted high boron alloy, shown with red x marks in Fig. 3a, were examined in the CSLM. Low boron samples, ~0.003 wt% B, were taken from the middle of the DS zone. Mid-boron samples, ~0.011 wt% B, were cut from the region at the start of the last zone, and high boron samples, ~0.133 wt% B, were from the middle of the last zone. With these three compositions, the phase transformations were investigated during heating and cooling of the samples. Upon heating, all samples saw a phase change occur between 921 °C and 959 °C, the $\alpha\text{-bcc}$ to $\gamma\text{-fcc}$ transition. The low boron samples saw melting at ~1560 °C corresponding to the expected liquidus temperature. The mid-boron and high boron samples saw the first melting occur between 1145 °C and 1165 °C at the eutectic structure. The metatectic reaction occurred at ~1381 °C for the mid-boron sample with significant amounts of liquid resolidifying upon heating, Fig. 6a. The high boron sample saw a phase change at ~1369 °C with only a slight amount of liquid resolidifying. During cooling, remelting in the mid-boron sample was seen at ~1358 °C, Fig. 6b. For the high boron sample, there was a small amount of remelting at ~1312 °C. Final solidification occurred

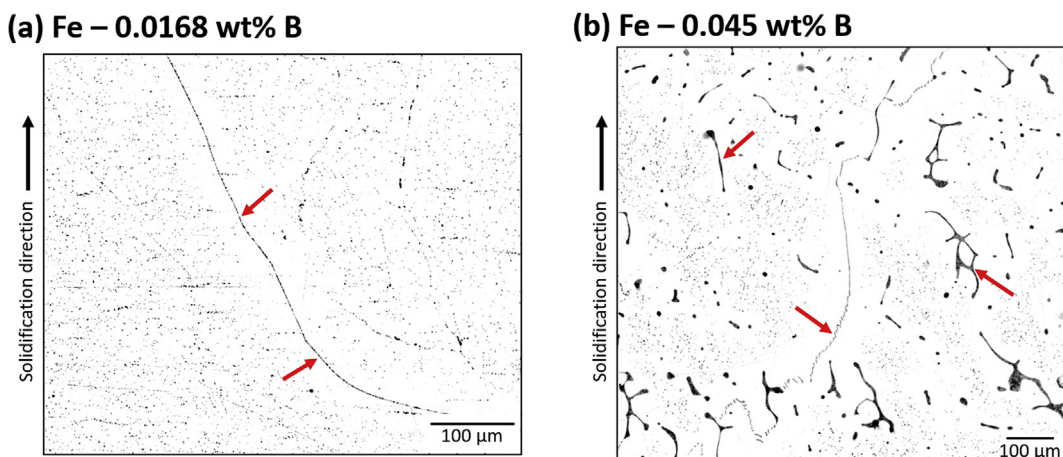


Fig. 5. Optical images of the polished zone melted (a) low boron alloy and (b) high boron alloy from the last zone to solidify with arrows highlighting the eutectic structure in each alloy.

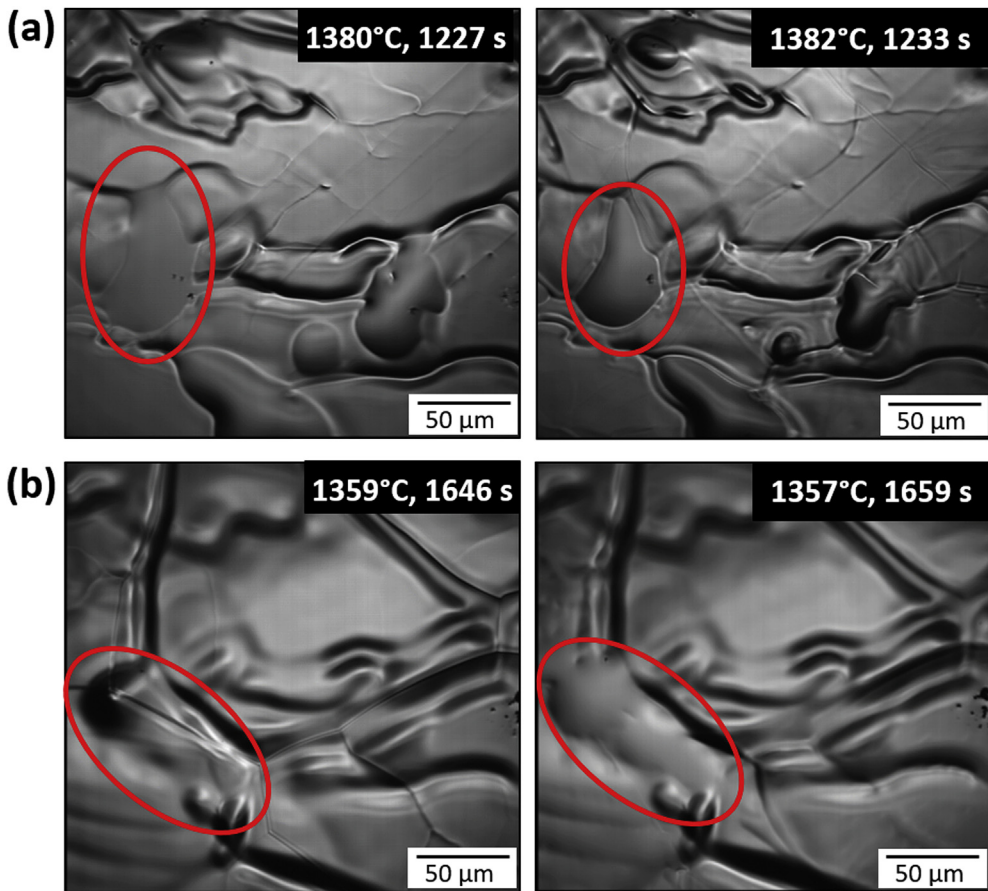


Fig. 6. Images collected from the CSLM during (a) heating and (b) cooling of the mid-boron sample containing ~0.133 wt% B. (a) The metatectic reaction during heating is evident as the liquid is seen to solidify as the temperature increased. (b) The metatectic reaction was also observed during cooling as the sample remelted with a decrease in temperature.

between 1045 °C and 1164 °C for the mid-boron and high boron samples with the high boron samples undergoing another phase change between 859 °C and 872 °C.

The high temperature phase transitions are superimposed on the Thermo-Calc predicted phase diagrams in Fig. 7 with the high boron samples, 0.133 wt% B, represented on the end of the partial phase diagrams. In the phase diagram produced with TCFE5, Fig. 7a, the mid boron sample is not predicted to remelt, but remelting was seen in the CSLM. This sample is predicted to remelt in the phase diagram generated with the TCFE8 diagram, Fig. 7b. However, the low boron sample is also predicted to remelt in this diagram, which did not occur in the small area examined in these experiments. Of these two diagrams, TCFE8 appears to better match the CSLM experimental results.

4. Discussion

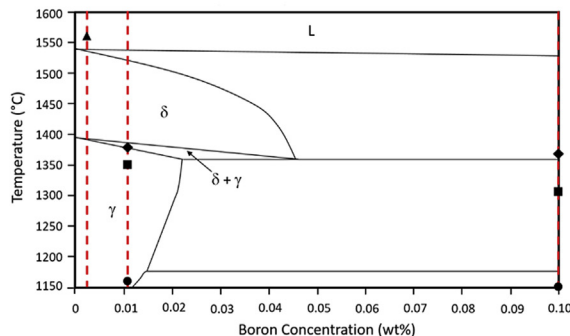
Various systems that undergo a metatectic reaction have been investigated to determine what type of microstructure is produced from the low temperature remelting. Some systems produce microstructure that include spherical particles located in the bulk of the primary grains. These spherical particles form when liquid nucleates in the center of grains as the metatectic reaction proceeds. This type of microstructure has been seen in various rare earth alloys and Cu-Sn alloys that undergo a metatectic reaction [18,19]. Another microstructure that is attributed to the metatectic reaction are thin films that form between primary and secondary phases, such as sulfide films forming in the Fe-S system [20,21]. For

the Fe-B system the observed morphology is similar to the spherical particles present in metatectic rare earth alloys and is proposed to form as follows.

Based on these previous studies and 1D Scheil solidification, the interdendritic microsegregation behavior for the last zone to solidify of the zone melted Fe-B ingots is predicted in Fig. 8 with the Thermo-Calc TCFE8 phase diagram. As the temperature is initially reduced in the fully liquid region, δ-bcc iron grows. The boron content in the δ-bcc phase increases along the δ-bcc solidus as the dendrite grows outward, highlighted in Fig. 8a. Once the metatectic temperature of 1384 °C is reached, remelting is predicted to occur in the prior δ-bcc dendrite where the boron content falls in the δ + γ region of the phase diagram, between 0.0025 and 0.0097 wt% B. This remelting within the δ-bcc phase is represented by the red dots in Fig. 8. Below the metatectic temperature, γ-fcc iron will solidify directly from the liquid. After 1175 °C, any remaining liquid will solidify as the γ + Fe₂B binary eutectic. Based on this analysis, the binary eutectic should be surrounded by a zone where no remelting occurs with the expected microstructure shown in Fig. 8b.

The observed experimental microstructures match the general predictions as shown in Fig. 9, but there were also some significant differences with respect to the measured phase fractions as listed in Table 3. For example, the areas that contain the spherical Fe₂B particles are assumed to correspond to the prior δ-bcc phase, and the white areas devoid of the particles located next to the eutectic are assumed to correspond to the prior, post-metatectic, γ-fcc phase. These are labeled in Fig. 9a. Quantitative microstructure

(a) TCFE5



(b) TCFE8

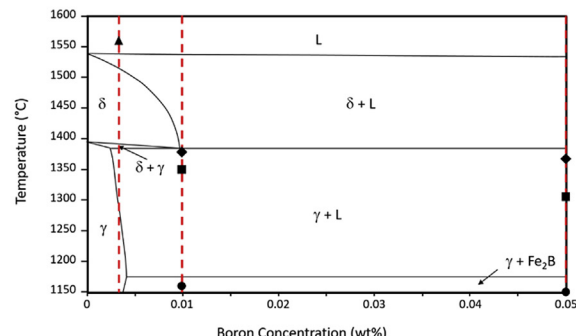
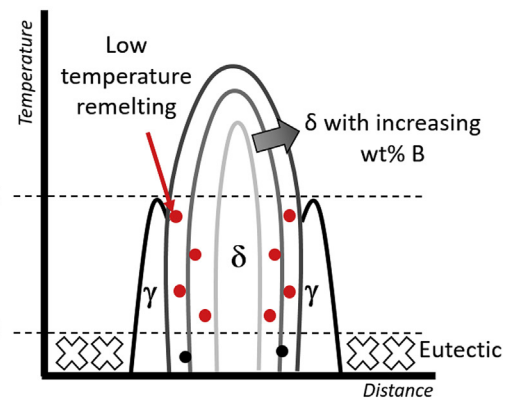
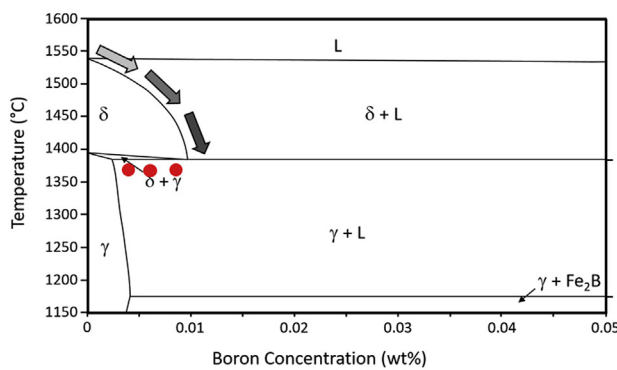


Fig. 7. The Thermo-Calc predicted Fe-B phase diagrams from (a) TCFE5 and (b) TCFE8 databases with the high temperature phase transitions observed in the CSLM marked at approximately the three sample compositions. The sample with the highest boron content contained ~0.133 wt% B, so it is represented at the end of the partial phase diagrams.

(a)



(b)

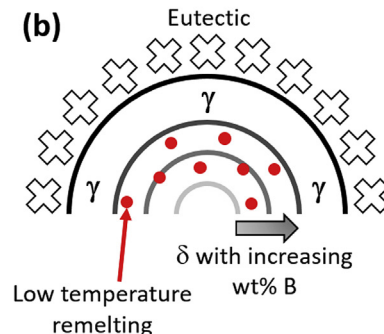


Fig. 8. (a) The predicted microstructure in the last zone to solidify of the zone melted ingots as temperature decreases, and (b) a transverse cross section of that predicted microstructure.

image analysis was utilized to determine the percent area of each phase from the high boron zone melted alloy [17]. The region corresponding to the prior δ-bcc phase was shaded black, as shown in Fig. 9b, allowing the fraction of the prior γ-fcc phase, the white area, to be calculated. Similarly, re-shading the prior δ-bcc phase to white allows the fraction of the eutectic microconstituent to be found. However, these area fractions compare poorly to the mass fractions calculated from the 1D Scheil equation, shown in Table 3.

The mismatch in the calculated and measured phase fractions could stem from the way the microstructure was predicted to form, specifically from the microstructural changes that occur due to the

metatactic reaction. One possibility is that some fraction of prior γ-fcc phase listed in Table 3 results from the $\delta \rightarrow \gamma + L$ metatactic reaction. Consider again the cored composition of the original δ dendrite shown in Fig. 10. Due to the steepness of the δ-solidus at the metatactic temperature, the outermost core of the δ dendrite will have a near-metatactic composition. However, this region will be in direct contact with the bulk liquid, and thus there is no need to nucleate the liquid for the metatactic reaction to proceed. As a result, the γ-fcc phase can grow at the expense of the δ-bcc phase along the solid/liquid interface. This is illustrated in Fig. 10. At the metatactic temperature, 1384 °C, the prior-δ dendrite will decrease

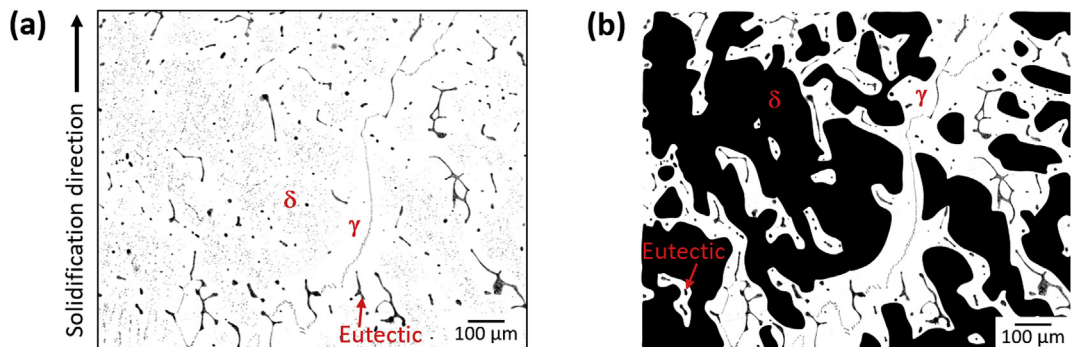


Fig. 9. (a) Optical image from the last zone to solidify of the high boron zone melted alloy. The δ -bcc phase, γ -fcc phase, and the eutectic structures are labeled. (b) The δ -bcc phase is covered in dark shapes to allow the area fraction of the γ -fcc phase to be determined using ImageJ. When those dark shapes are converted to white, the area fraction of the eutectic structure can then be determined.

Table 3

The calculated phase fractions from the 1D Scheil equation and the area fractions from the image analysis for each phase in the last zone of the zone melted high boron alloy, $C_0 = 0.21$ wt% B.

	1D Scheil Analysis	Image Analysis
Fraction Solid (%)	% Area	
Prior δ -bcc iron	90.5	50 ± 4.9
Post metatactic γ -fcc iron	4.27	47 ± 4.9
Eutectic	5.19	3.3 ± 0.12
Spherical areas (assumed metatactic remelting) within the grains	—	1.71 ± 0.12

in size as the outer layer remelts in the presence of the bulk liquid.

On the other hand, the center of the δ -bcc dendrite has a lean hypometatactic composition, and γ -fcc can nucleate and grow from the parent δ -bcc phase in the solid state. Once the metatactic temperature is reached upon cooling, the remaining δ -bcc phase is physically separated from the bulk liquid, and the metatactic reaction results in the remelting within the δ -bcc phase. Shown in Fig. 10b is a schematic transverse cross section of the microstructure detailing where the remelting occurs along with the increase in boron content from the center of the dendrite. Since the image analysis only accounts for the δ -bcc phase that contained spherical particles, this could explain why the amount of measured δ -bcc is lower than the predicted amount.

Another comparison between the experimental optical images and the predicted phase diagrams is a measurement of the amount of liquid that undergoes the metatactic reaction. Using the data

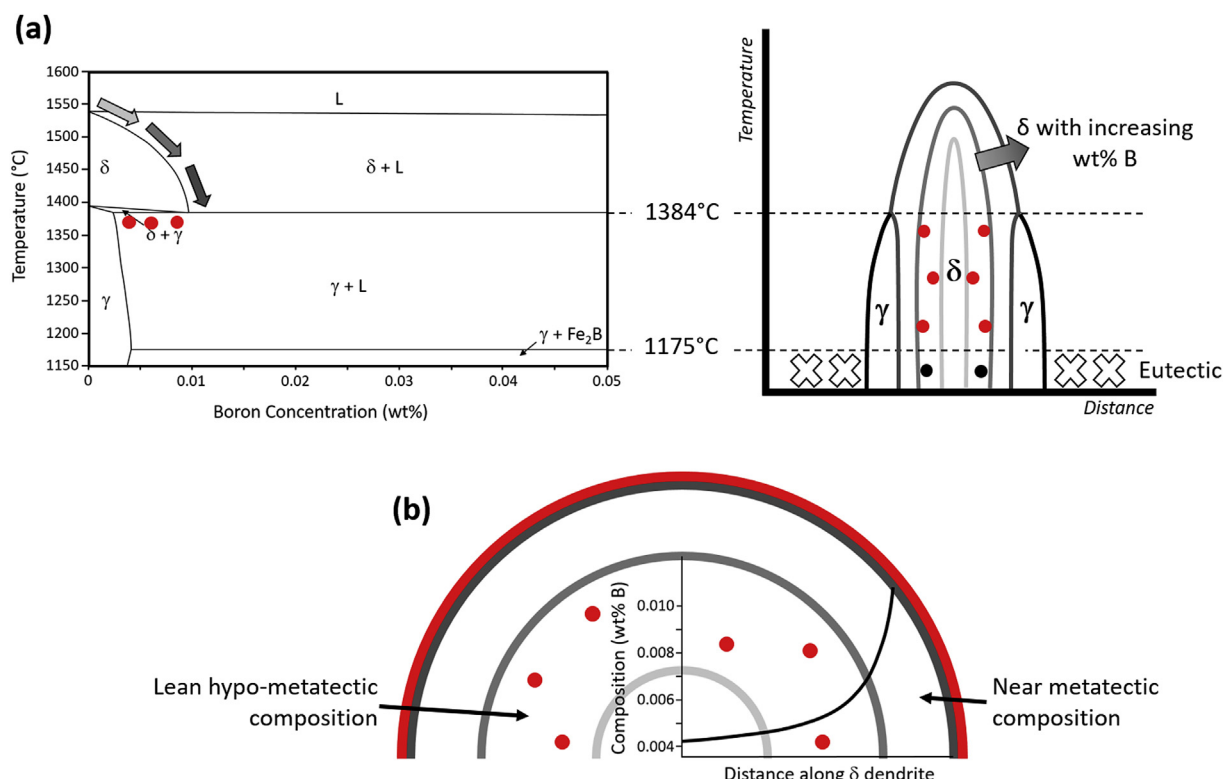


Fig. 10. (a) The development of the microstructure seen in the last zone to solidify of the zone melted ingots as the temperature is decreased. (b) Transverse cross section of the microstructure at the metatactic reaction. The composition profile details the radial increase in boron concentration that leads to two different remelting locations.

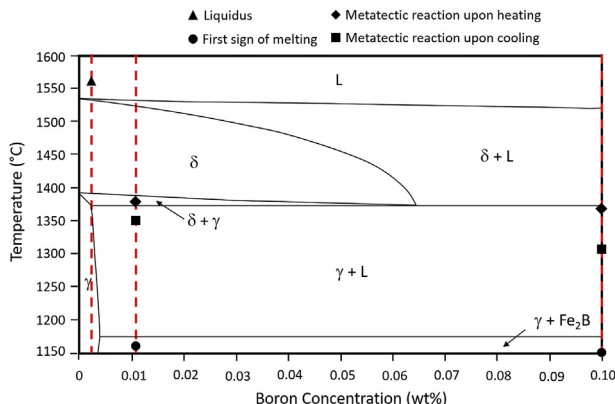


Fig. 11. Modifications to the predicted Fe-B binary phase diagram based on experimental data. The high temperature phase transitions observed in the CSLM are marked at approximately the three sample compositions. The sample with the highest boron content contained ~0.133 wt% B, so it is represented at the end of the partial phase diagram.

from TCFE8 in Table 1, the mass fraction of liquid that forms due to the metatectic reaction is 0.32%, and this corresponds to a volume fraction of 0.39% assuming the density of γ -fcc and liquid to be 8.6 and 6.98 g/cm^3 , respectively. However, from quantitative microstructural measurements of the spherical regions corresponding to the low temperature remelting, as highlighted in Fig. 9, a volume fraction of 1.71% was found. From these values, the composition of the metatectic reaction can be modified. For example, using $C_o = 0.21 \text{ wt\% B}$, the average composition in the last zone to solidify of the high boron alloy, the mass fraction that solidifies as δ -bcc is 90.5%, shown in Table 2. If the measured volume fraction of the liquid from the metatectic reaction is assumed to be associated with the spherical boride regions, then a metatectic composition of $C_R = 0.034 \text{ wt\% B}$ is required. If it is assumed that only 50% of the spherical boride region corresponds to approximately half the amount of δ -bcc iron that solidified, from Table 3, then a composition of $C_R = 0.064 \text{ wt\% B}$ is required to match the 1.71% measured for the spherical boride regions. If these calculations are repeated using $C_o = 0.133 \text{ wt\% B}$, the single bulk compositional measurement from the last zone shown in Fig. 3b, the values for C_R are similar and range from 0.032 to 0.061 wt%. All of these cases result in a metatectic composition greater than that given by TCFE8 database. Utilizing the values of composition and temperatures from the CSLM experiments and quantitative microstructural analysis of the zone melted Fe-B alloys, modifications to the Fe-B phase diagram are shown in Fig. 11.

5. Conclusions

This study showed that boron segregation was successfully controlled through levitation zone melting providing an experimental method to examine the predicted phase diagrams. Microstructural evidence of a metatectic reaction was observed in both optical images of the zone melted ingots and in the CSLM experiments. Through these results, it is predicted that the metatectic reaction occurs through two different microstructural changes. The outer core of the δ -bcc dendrite that is approximately at the

metatectic composition will remelt along the solid/liquid interface while the inner core of the dendrite with lower amounts of boron will nucleate liquid within the δ -bcc phase resulting in spherical boride particles. Measuring the amount of those particles allows for modifications to the predicted phase diagram. Based on the experimental results, the metatectic reaction occurs at $C_s = 0.0025 \text{ wt\% B}$, $C_L = 2.0 \text{ wt\% B}$, and C_R ranging from approximately 0.03 to 0.06 wt% B.

Acknowledgements

The authors would like to thank the East Chicago (USA) Center of ArcelorMittal Global R&D for the gift that supported this work along with the raw materials, bulk composition measurements, and the use of their confocal scanning laser microscope. We would also like to thank Dr. Chris Gilpin for his assistance with EDX.

References

- [1] S. Keeler, M. Kimchi, Advanced High-strength Steels Application Guidelines Version 5.0, 2014, [https://doi.org/10.1016/S1644-9665\(12\)60197-6](https://doi.org/10.1016/S1644-9665(12)60197-6).
- [2] C.M. Tamarelli, AHSS 101: the Evolving Use of Advance High-strength Steel for Automotive Applications, 2011.
- [3] K.E. Blazek, O. Lanzi, H. Yin, The Effect of Boron Additions on the Solidification of Steel during Continuous Casting, Part I, AISTech, Pittsburgh, 2008.
- [4] H. Yin, K. Blazek, O. Lanzi, "In-situ" observation of remelting phenomenon after solidification of Fe-B alloy and B-bearing commercial steels, ISIJ Int. 49 (2009) 1561–1567, <https://doi.org/10.2355/isijinternational.49.1561>.
- [5] K.E. Blazek, O. Lanzi, H. Yin, Boron effects on the solidification of steel during continuous casting, Rev. Métallurgie 105 (2008) 609–625.
- [6] T. Van Rompaey, K.C.H. Kumar, P. Wollants, Thermodynamic optimization of the B–Fe system, J. Alloys Compd. 334 (2002) 173–181.
- [7] O. Kubaschewski, Iron-binary Phase Diagrams, Springer-Verlag, Berlin Heidelberg, Dusseldorf, 1982, <https://doi.org/10.1007/978-3-662-08024-5>.
- [8] J.O. Andersson, T. Helander, L. Hoglund, P.F. Shi, B. Sundman, Thermo-calc & DICTRA, computational tools for materials science, Calphad 26 (2002) 273–312.
- [9] Thermo-calc Software TCFE5 Steels/Fe alloys database version 5 (Accessed 12 March 2017).
- [10] Thermo-calc Software TCFE8 Steels/Fe alloys database version 8 (Accessed 12 March 2017).
- [11] B.F. Oliver, A levitation zone melter for larger diameter bars with positive process control, Trans. Metall. Soc. AIME 227 (1963).
- [12] R.D. Reviere, B.F. Oliver, D.D. Bruns, Computer controlled containerless processing of high temperature intermetallic compounds, Mater. Manuf. Process. (1989) 103–131, <https://doi.org/10.1080/10426918908956275>.
- [13] D.R. Johnson, X.F. Chen, B.F. Oliver, R.D. Noebe, J.D. Whittenberger, Processing and mechanical properties of in-situ composites from the NiAl–Cr and the NiAl–(Cr, Mo) eutectic systems, Intermetallics 3 (1995) 99–113.
- [14] B.F. Oliver, B.Y. Huang, W.C. Oliver, Containerless growth of large single crystals of TiAl, Scr. Metall. 22 (1988) 1405–1408.
- [15] W.G. Pfann, Principles of zone melting, Trans. Am. Inst. Min. Metall. Eng. 194 (1952) 747–753.
- [16] H. Chikama, H. Shibata, T. Emi, M. Suzuki, "In-situ" real time observation of planar to cellular and cellular to dendritic transition of crystals growing in Fe-C alloy melts, Mater. Trans. JIM 37 (1996) 620–626, <https://doi.org/10.2320/matertrans1989.37.620>.
- [17] C.A. Schneider, W.S. Rasband, K.W. Eliceiri, NIH Image to ImageJ: 25 years of image analysis, Nat. Methods 9 (2012) 671–675, <https://doi.org/10.1038/nmeth.2089>.
- [18] R. Ferro, A. Saccone, S. Delfino, A.M. Cardinale, D. Maccio, Inverse melting in binary systems: morphology and microscopy of catactic alloys, Metall. Mater. Trans. B 27B (1996) 979–986.
- [19] M. Stier, M. Rettenmayr, Microstructural evolution in near-metatectic Cu-Sn alloys, J. Cryst. Growth 311 (2008) 137–140, <https://doi.org/10.1016/j.jcrysgro.2008.10.033>.
- [20] H. Fredriksson, J. Stjerndahl, On the formation of a liquid phase during cooling of steel, Metall. Trans. B 6B (1975) 661–663.
- [21] H. Fredriksson, J. Stjerndahl, The influence of the ferrite to austenite transformation on the formation of sulfides, Metall. Trans. A 8A (1977) 1107–1115.